Friction **11**(11): 2091–2106 (2023)
https://doi.org/10.1007/s40544-022-0722-6
ISSN 2223-7690
CN 10-1237/TH
RESEARCH ARTICLE

Synergistically assembled RGO/Si_3N_4 whiskers hybrid aerogels to endow epoxy composites with excellent thermal and tribological performance

Yongjun ZHOU[1], Yuanya ZHANG[1], Meng LIU[2,3], Yanling WANG[2,3], Junya YUAN[2,*], Xuehu MEN[1,*]

[1] *School of Materials and Energy, Lanzhou University, Lanzhou 730000, China*

[2] *State Key Laboratory of Solid Lubrication, Lanzhou Institute of Chemical Physics, Chinese Academy of Sciences, Lanzhou 730000, China*

[3] *Center of Materials Science and Optoelectronics Engineering, University of Chinese Academy of Sciences, Beijing 100049, China*

Received: 09 March 2022 / Revised: 17 May 2022 / Accepted: 09 November 2022

Abstract: Epoxy resin (EP) composites with satisfactory thermal and tribological performance are highly required for engineering moving components. However, the simple addition of fillers leaded to the serious filler agglomeration and limited promotion in tribological properties. In this work, we constructed a new kind of three-dimensional (3D) reduced graphene oxide (RGO)/Si_3N_4 hybrid aerogel for EP composites, which was prepared by a facile hydrothermal self-assembly method followed by freeze-drying technique. As a result, the dispersibility of Si_3N_4 whiskers was greatly improved through wrapping of polydopamine–polyethyleneimine copolymer (PDA–PEI) copolymer and physical spacing of 3D skeleton. Furthermore, benefiting from the synergistic effect of RGO and Si_3N_4@PDA–PEI in the thermal network, the thermal conductivity of RGO/Si_3N_4 hybrid aerogel (GSiA)–EP increased by 45.4% compared to that of the neat EP. In addition, the friction coefficient and wear rate of GSiA–EP decreased by 83.7% and 35.8%, respectively. This work is significant for opening a tribological performance enhancement strategy though constructing 3D hybrid architecture.

Keywords: three-dimensional (3D) hybrid structure; reduced graphene oxide (RGO)/Si_3N_4 hybrid aerogel; thermal properties; tribological properties; wear mechanism; synergistic effect

1 Introduction

Epoxy resin (EP) is widely employed as mechanical system in the aerospace field due to its low cost, light weight, and excellent processability [1–3]. Owing to the special environment of high temperature and high altitude, the EP urgently need to further satisfy the demand for excellent thermal properties, outstanding mechanical properties, and good tribological performance simultaneously [4–6]. Thus, numerous attentions have been focused on adding the high-performance micro/nanofillers into the EP matrix, such as carbon nanostructures, diamond-like carbon, and ceramic phases [7–10]. Among them, the carbon nanostructures, including zero-dimensional carbon nanoparticles (CNPs), one-dimensional carbon tubes (CNTs), and two-dimensional graphene oxide sheets (GO) have been evaluated as a good candidate because of its excellent thermal conductivity and outstanding lubricating properties [11–14]. However, due to the surface effect, the fillers agglomeration, resulting in uneven dispersion in polymer matrix, prevents these carbon nanostructures from reaching their full potential. In addition, these fillers are hard to interlaced together to construct continuous thermal networks into composites. As a result, they cannot dissipate the friction heat in time, leading to an extremely high instantaneous interface temperature and the decline of epoxy matrix [15–18].

Recently, graphene aerogels (GAs), having a three-

* Corresponding authors: Junya YUAN, E-mail: yuanjunya@licp.cas.cn; Xuehu MEN, E-mail: menxh2018@163.com

dimensional (3D) honeycomb-like structure, can solve these adverse factors perfectly with interconnected porous architectures, low bulk density, and high porosity [19–21]. However, due to the weak connection and stacking between GO flakes, the concentration of GO dispersion had certain limitations during the fabrication process of GAs. Moreover, single GAs has the inevitable structural defects, leading to incomplete thermal conduction pathways and mechanical properties [23–25]. As a result, the researchers are committed to embedding different-dimensional reinforcing materials into the GAs to improve the mechanical stability and thermal properties of GAs as anchoring materials [26, 27]. Apparently, taking 3D hybrid aerogel as the reinforcing skeleton of EP matrix, the thermal and mechanical properties as well as tribological properties of EP composites could be improved effectively.

The ceramic-phase materials, including SiC nanowires, and Si_3N_4 ceramic whiskers, are often employed to improve the thermal and mechanical properties of polymer composites because of their high thermal properties, outstanding mechanical strength, and hardness [28–32]. Among them, Si_3N_4 ceramic whiskers, with special aspect ratio between powder and fiber, attracted great attentions to enhance the thermal, mechanical properties of polymer composites. However, the dispersion of Si_3N_4 whiskers is not fascinating due to the lack of active groups on the surface, resulting in the agglomeration and precipitation. Numerous studies are devoted to improving the dispersibility of Si_3N_4 whiskers in composites via surface modification [28, 29, 33]. Recently, as a surface modifier without any host selectivity, the polydopamine–polyethyleneimine copolymer (PDA–PEI) has demonstrated its immense capability and potential for modifying the surface of Si_3N_4 whiskers [34, 35]. Besides, interspersing or embedding the modified Si_3N_4 whiskers between the voids of GAs via hydrogen bonding, covalent grafting, and mechanical interlocking could further alleviate the agglomeration and precipitation [36, 37]. In this way, it can be assumed that graphene sheets could act as physical spacers to separate the Si_3N_4 whiskers. Meanwhile, the incorporating of one-dimensional Si_3N_4 whiskers into GAs can strengthen the skeleton of GAs by serving as anchoring bridges and build continuous heat-dissipation highways into the 3D conduction network. Most importantly, as a reducing agent, the PDA–PEI coated onto the Si_3N_4 whiskers surface can promote the fabrication of GAs during hydrothermal reduction to some extent. Thus, the 3D graphene aerogels and one-dimensional Si_3N_4 whiskers may have a potential synergistic effect on the tribological properties of EP composites. Moreover, the above assumption has not been investigated yet, and it is necessary to attempt further in the present research.

Based on above motivation, in this work, for the first time the Si_3N_4 whiskers were modified with the PDA–PEI copolymer, and a 3D porous graphene aerogel-supported Si_3N_4@PDA–PEI (reduced graphene oxide (RGO)/Si_3N_4 hybrid aerogel) was prepared via a facile and scalable hydrogel route. Finally, the epoxy resin was poured into the hybrid aerogel by vacuum-assisted impregnation method to prepare the EP composites. The composition and structure of obtained RGO/Si_3N_4 hybrid aerogel were thoroughly investigated via scanning electron microscopy (SEM), transmission electron microscopy (TEM), X-ray diffraction (XRD), Fourier transform infrared spectrometer (FTIR), and X-ray photoelectron spectroscopy (XPS). The skeleton structure of RGO/Si_3N_4 hybrid aerogel in epoxy resin were explored by optical microscope. The obtained RGO/Si_3N_4 hybrid aerogel–EP composites presented excellent thermal, mechanical, and tribological properties. Moreover, the tribological behavior and wear mechanism of EP composites were further investigated in detail via analyzing the wear surface and transfer film. This work opens a new avenue to promote the tribological performance of polymer composites by constructing 3D hybrid aerogel.

2 Experimental

2.1 Materials

Si_3N_4 whiskers (with a diameter of 0.1–0.6 μm and a length of 5–7 μm) were purchased from Aladdin Co., Ltd. Few-layer graphene oxide platelets (GO, with a lateral size between 1 and 10 μm) were obtained from Shanghai Meryer Biochemical Co., Ltd. Shanghai Energy Chemical Co., Ltd. provided the dopamine hydrochloride (DA). PEI and L-ascorbic acid (LAA) were obtained by Shanghai Macklin Biochemical Co., Ltd. Nantong Xingchen Synthetic Material Co.,

Ltd. supplied the EP (E-51) and the curing agent triethylenetetramine ($C_6H_{18}N_4$).

2.2 Preparation of RGO/Si_3N_4 hybrid aerogel and GSiA–EP composites

Figure 1(a) displayed the whole fabrication process of the GSiA–EP composites. Firstly, Si_3N_4 whiskers, DA, and PEI were dispersed into 500 mL tris buffer solution by ultrasonicating for 8 h (all the sample concentrations were 2 mg/mL). The obtained suspension was centrifuged and the collected sediment was alternately washed by deionized water and ethanol for several times, and followed by drying in vacuum for 24 h to obtain the Si_3N_4@PDA–PEI whiskers.

Afterward, a certain amount of Si_3N_4@PDA–PEI whiskers were dispersed into 25 mL GO dispersion (3mg/mL) by magnetic stirring for 12 h. And then 0.300 g LAA was dispersed into the above solution by re-sonicating for 1 h. Then, the prepared mixture was transferred into a sealed bottle and hydrothermally reduced for 2 h in an oven at 80 °C to obtain the RGO/Si_3N_4 hybrid hydrogel. The self-assembled hybrid hydrogel was repeatedly washed by deionized water to remove the impurities. Subsequently, the hybrid hydrogel was first frozen with liquid nitrogen for 5 min, and followed by lyophilizing for 24 h in a freeze-drier to obtain the RGO/Si_3N_4 hybrid aerogel (GSiA). The RGO/Si_3N_4 hybrid aerogels with different mass ratio (the mass ratio of RGO flakes and Si_3N_4@PDA–PEI whiskers were designed as 2:1, 1:1, and 1:2) were coded as $GSiA_1$, $GSiA_2$, and $GSiA_3$, respectively. In addition, the neat graphene aerogels (GA) without Si_3N_4@PDA–PEI whiskers were prepared by the same procedure via using different concentration of GO dispersion (1, 2, 3, and 4 mg/mL) and designated as GA_1, GA_2, GA_3, and GA_4, respectively.

Finally, the EP and $C_6H_{18}N_4$ (the mass ratio was 3:1) were magnetic stirred for 10 min. Sequentially, the GSiA was immersed into the above mixture under vacuum for 0.5 h. The products were left at room temperature for 4 h and kept for 6 h in an oven at 100 °C in order to prepare the RGO/Si_3N_4 hybrid aerogel–EP composites (GSiA–EP) composites. The GSiA–EP composites with different GSiA ($GSiA_1$, $GSiA_2$, and $GSiA_3$) were designated as $GSiA_1$–EP, $GSiA_2$–EP, and $GSiA_3$–EP, respectively. Meanwhile, the RGO aerogel–EP composites (GA–EP) were fabricated in the same way. The GA–EP composites with different GA (GA_2, GA_3, and GA_4) were designated as GA_2–EP, GA_3–EP, and GA_4–EP, respectively. As a contrast, the GO/Si_3N_4–EP composites were prepared by simply mixing GO and Si_3N_4 whiskers into the EP matrix.

2.3 Characterization

SEM (JSM-6701F, Japan) and HR-TEM (Tecnai F30, America) were used to observe the morphology and microstructure of the samples. The chemical component of the samples was characterized using XRD (D8 Discover 25), FTIR (NEXUE 670), XPS (Kratos AXIS Ultra DLD), and micro-Raman spectroscopy.

The optical microscope (OM, OLYMPUS UC90) was taken to explore the distribution of RGO/Si_3N_4 hybrid aerogel in the epoxy resin. The thermal conductivities of the composites were obtained via laser thermal conductivity apparatus (LFA-457) and PerkinElmer Pyris diamond thermal analyzer performed the thermal gravimetric analysis (TGA) under N_2 atmosphere. The thermal imaging camera (Fotric323pro) was conducted for monitoring the real-time temperature of the composites. The hardness experiments were measured by Vickers microhardness tester (HVT-1000A) and the hardness of all samples were performed at least five tests to calculate the average values. The friction and wear tests were performed by the ball-on-disk apparatus (MS-T3001, load 10 N, speed 200 r/min). The wear volume was investigated by 3D profilometer (MicroXAM-800, America) and the specific wear rate W_S was calculated by the formula (1):

$$W_S = \Delta V \cdot F^{-1} \cdot L^{-1} \quad (1)$$

where ΔV is the wear volume; F is the applied load; and L is the sliding distance. All key experiment results were measured three times and the average values were adopt to minimize the error.

3 Results and discussion

3.1 Characterization of GSiA and GSiA–EP composites

The synthetic route of RGO/Si_3N_4 hybrid aerogel via

combing the Si_3N_4 whiskers and RGO sheets was exhibited in Fig. 1. According to the previous research work [34], owing to the hydrophilicity of oxygen-containing group, the helical carbon nanotubes could be attached to the GO nanosheet surface in the water solution. On this account, the Si_3N_4@PDA–PEI whiskers could be evenly parasitized in the GO sheets because of the reactive groups on Si_3N_4@PDA–PEI whiskers surface in aqueous dispersion. After the hydrothermal procedure, the RGO hydrogels with or without Si_3N_4@PDA–PEI whiskers kept a cylindrical shape and displayed a slight volume shrinkage except for the GO concentration of 1 mg/mL (Figs. S1 and S2 in the Electronic Supplementary Material (ESM)). Subsequently, the freeze-drying method was taken to obtain the RGO/Si_3N_4 hybrid aerogels and then the RGO/Si_3N_4–EP composites were obtained by vacuum-assisted impregnation. As showed in Fig. 1(b), the PDA–PEI copolymer were obtained by the self-polymerization of DA and the copolymerization with PEI. Through π–π accumulation and hydrogen bonding, the Si_3N_4 whiskers were coated by the PDA–PEI copolymer (Fig. S3 in the ESM) and then the dispersion of Si_3N_4@PDA–PEI whiskers in deionized water was greatly improved (Fig. S4 in the ESM). In the process of hydrothermal reduction (Fig. 1(c)), the –OH functional groups provided by PDA–PEI and LAA were changed into ketones. Meanwhile, the oxygen-containing functional groups on GO flakes (i.e., –OH and –COOH) were partly removed and the sp^2 lattice structure was restored to some extent. The light RGO/Si_3N_4 hybrid aerogels with the weight of 0.021 g could be allowed to stand on a dandelion flower and support a load of 500 g without collapse (Fig. 1(d)). Figure 1(e) displayed the possible binding force in RGO/Si_3N_4–EP composites during the curing reaction. In addition to the π–π accumulation and hydrogen bonding, the active $–NH_2$, from current agent and PDA–PEI copolymer, undergone an epoxy ring-opening reaction with the epoxy group on the EP matrix and esterification reaction with the residual groups (–COOH) on RGO sheets surface to form a covalent bond. As a result, the Si_3N_4@PDA–PEI whiskers could be stably embedded into the 3D skeleton constructed by RGO sheets and the binding strength between EP matrix and RGO/Si_3N_4 hybrid aerogel could be improved markedly.

The internal porous structures of RGO aerogel and RGO/Si_3N_4 hybrid aerogel were comparatively investigated by the SEM and TEM images. Without

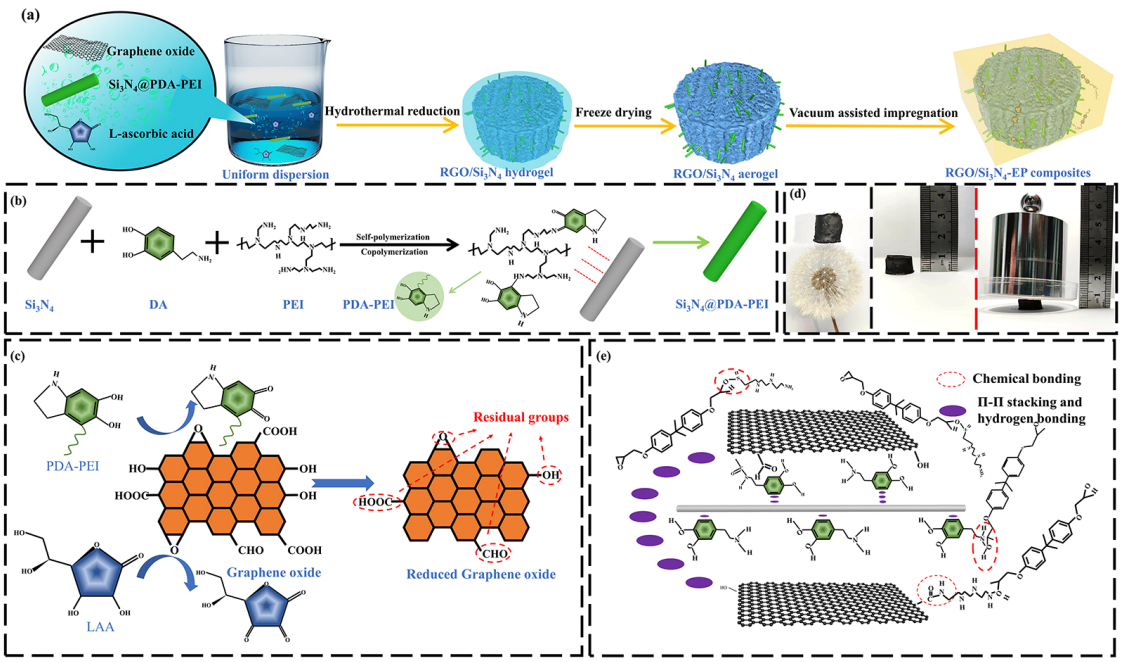

Fig. 1 (a) Schematic flowchart of preparing the GSiA–EP composites; (b) reaction scheme of the synthesis of Si_3N_4@PDA–PEI whiskers; (c) schematic illustration of hydrothermal reduction of RGO/Si_3N_4 hybrid aerogel; (d) digital images of GSiA; and (e) the possible binding force of RGO/Si_3N_4–EP composites.

Si_3N_4@PDA–PEI whiskers, the GA_3 displayed the traditional cellular graphene walls, which were thin and soft (Figs. 2(a)–2(c)). Meanwhile, it could be observed in Figs. 2(d) and 2(e) that Si_3N_4@PDA–PEI whiskers were uniformly parasitized in the cross-linked network, suggesting that the RGO sheets served as a good dispersant for Si_3N_4 whiskers. However, the pore size of $GSiA_1$ was bigger than that of neat RGO aerogel and the cellular graphene walls turned more solid and thick (Figs. 2(d) and 2(e)), implying that the Si_3N_4@PDA–PEI whiskers could also protect RGO sheets from stacking to some extent. Furthermore, the high-magnification SEM (HM SEM) images of $GSiA_1$ showed that the Si_3N_4@PDA–PEI whiskers welded the holes (Fig. 2(f)), as well as was wrapped by RGO sheets entirely (Fig. 2(g)) or embedded incompletely (Fig. 2(h)) throughout the RGO cross-linked skeleton. From Fig. 2(i), both the continuous RGO wrinkles and PDA–PEI co-deposition coating could be observed in the TEM images, corresponding to the 3D hybrid structure of RGO/Si_3N_4. However, as the content of Si_3N_4@PDA–PEI whiskers increased, the more Si_3N_4@PDA–PEI whiskers in $GSiA_2$ were exposed outside the skeleton compared to the $GSiA_1$ (Figs. 2(j) and 2(k)). The aggregation of Si_3N_4@PDA–PEI whiskers got much worse and then damaged the structure uniformity due to the excessive contents (Figs. 2(m) and 2(m_1)).

The chemical composition of RGO/Si_3N_4 hybrid aerogel was displayed in Fig. 3. It can be seen that the XRD pattern of Si_3N_4 whiskers have a good agreement with β-phase Si_3N_4 [34]. When GO sheets were reduced to GA, the characteristic peak appearing at 2θ of 9.6° corresponding to (002) disappeared and a new broad peak occurring at 2θ of 25° corresponding to (100) could be observed, indicating the effective removal of oxygen-containing functional groups and poor ordering of RGO sheets [22, 38]. Meanwhile, the XRD

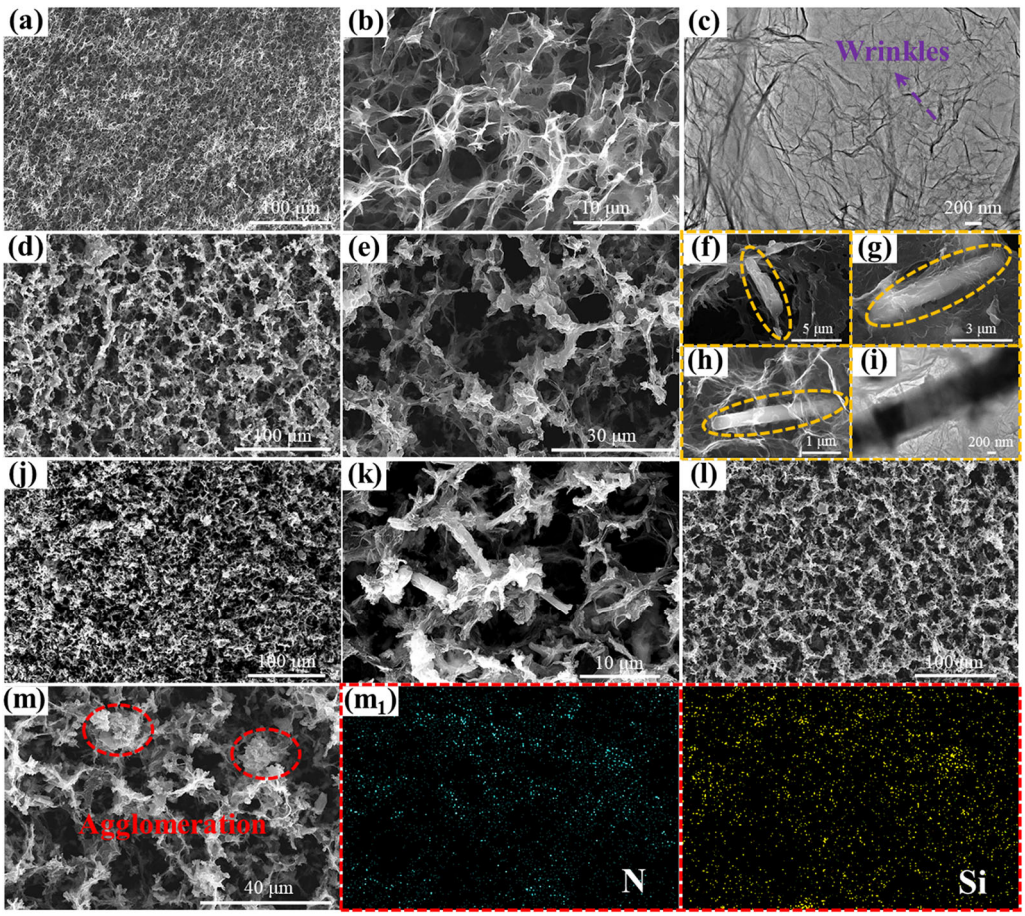

Fig. 2 SEM images and high-magnification SEM images of (a, b) GA_3, (d, e) $GSiA_1$, (j, k) $GSiA_2$, and (i, m) $GSiA_3$; TEM images of (c) GA and (i) $GSiA_1$; (f–h) HM SEM images of $GSiA_1$; and (m_1) EDS elemental mapping images of $GSiA_1$.

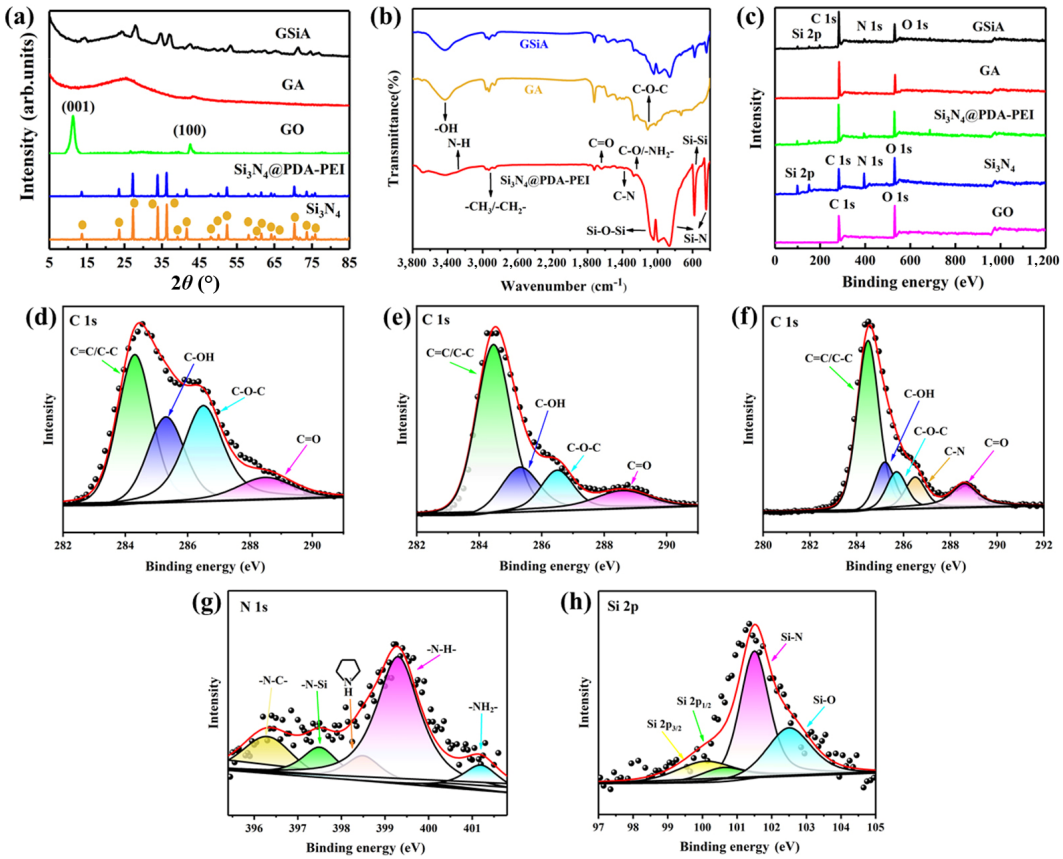

Fig. 3 (a) XRD patterns, (b) FTIR spectra, and (c) XPS survey spectra of Si_3N_4, Si_3N_4@PDA–PEI, GO, GA, and $GSiA_1$; high-resolution XPS spectrum of C 1s for (d) GO, (e) GA_3, and (f) $GSiA_1$; high-resolution XPS spectrum of (g) N 1s and (h) Si 2p for the Si_3N_4@PDA–PEI in $GSiA_1$.

pattern of RGO/Si_3N_4 hybrid aerogel simultaneously presented the characteristic peaks of RGO and Si_3N_4 whiskers. Figures 3(c) and S5 in the ESM further presented the FTIR spectra of aerogel and Si_3N_4 samples. The broad band between 3,200 and 3,600 cm^{-1} could be attributed to the –OH asymmetric stretching peak of GA. Two typical absorption peaks of Si_3N_4 were clearly observed at 400–600 cm^{-1} and 800–1,100 cm^{-1}, corresponding to the bending and stretching vibration of Si–N bond, respectively. Meanwhile, compared to the unmodified Si_3N_4 whiskers, the FTIR spectra of Si_3N_4@PDA–PEI whiskers exhibited the stronger –OH asymmetric stretching peak at 3,436 cm^{-1}, and the N–H absorption peak at 3,270 cm^{-1}. In addition, the new C=O, C–N, C–O/–NH_2 characteristic absorption peaks at 1,727, 1,388, and 1,274 cm^{-1}, respectively, were attributed to the PDA–PEI co-deposition coating [36]. In addition, both the Si_3N_4 whiskers and GA characteristic absorption peaks could be well discerned in the spectrum of RGO/Si_3N_4 hybrid aerogel, suggesting the successful assembly of RGO sheets and Si_3N_4@PDA–PEI whiskers.

The chemical bond type of RGO/Si_3N_4 hybrid aerogel sample was further analyzed by XPS measurements. As could be seen from Fig. 3(c), the C 1s and O 1s signals presented in the spectrum indicated the Si_3N_4 whiskers with weak oxidation. While there was a significant reduction of Si 2p and N 1s signals and enhancement of C/O ratio for Si_3N_4@PDA–PEI owing to the co-deposition of the PDA–PEI coating [36]. As for GO sheets, the C1s spectra was resolved into four component peaks C=C/C–C (284.3 eV), C–OH (285.2 eV), C–O–C (286.5 eV), and C=O (288.6 eV) (Fig. 3(d)). As a contrast, C–OH component in GA became weak, revealing the incomplete reduction of GO sheets in GA (Fig. 3(e)). Meanwhile, a new C–N (285.7 eV) bond peak appeared in GSiA accounting for the PDA–PEI co-deposition coating (Fig. 3(f)). According to the N 2p spectrum for GSiA, except for the N–Si (397.5 eV), –NH_2 (401.5 eV), –N–C–

(395.7 eV), and –N–H (399.8 eV) peaks could also be found due to the PDA–PEI coating. Moreover, the high-resolution spectrum of Si 2p could be divided into three peaks Si–N (101.9 eV), Si–O–Si (102.3 eV), and Si–C (101.2 eV) (Fig. 3(h)). All these results indicated the effective coating of PDA–PEI for Si_3N_4 whiskers and successful assembly of Si_3N_4 and GO sheets in GSiA.

In order to evaluate the dispersion of RGO/Si_3N_4 hybrid aerogel with 3D structure in the epoxy matrix, the optical microscopy images and SEM cross-sectional morphologies of the EP composites were exhibited in Fig. 4. As shown in Figs. 4(a)–4(d), it could be clearly seen that there existed a continuous and interconnected RGO/Si_3N_4 hybrids with 3D structure in EP composites. By a contrast, the obvious agglomeration of GO sheets and Si_3N_4 whiskers could be found in Figs. 4(e) and 4(f). Moreover, the uneven granular particulates, consisting of agglomerated GO sheets and Si_3N_4 whiskers, were exposed to the cross-sectional surface of the GO/Si_3N_4–EP (Fig. 4(i)), suggesting that the GO sheets and Si_3N_4 whiskers presented a poor dispersion in the epoxy resin by simple mechanical blending. In the meanwhile, compared to the pure epoxy resin with river-like patterns, the cross-sectional surface of GSiA–EP became visibly rough, which indicated the RGO/Si_3N_4 hybrids constructed a 3D cross-linking network inside the resin and then limited the brittle fracture of epoxy resin effectively (Figs. 4(g) and 4(h)).

3.2 Thermal properties

Figure 5 exhibited the TGA curves and the thermal conductivity to investigate the thermal stability and heat conduction performance of EP composites. It could be found from Fig. 5(a) that the TGA curves between neat EP and EP composites had the similar change trend, suggesting the analogous thermal decomposition behaviors. While it could be found that the temperatures of GA_3–EP and $GSiA_1$–EP for a 5 wt% mass loss increased by 2.1 and 5.1 °C compared to that of neat EP, respectively. It was due to the lamellar barrier effect of RGO sheets and the 3D developed physical blocking structure of GSiA that the escape of the volatile pyrolysis products could be retarded [39]. Moreover, the Si_3N_4@PDA–PEI whiskers in GSiA could combine with RGO sheets to produce an even strong interfacial interaction with EP matrix and further limit the chain segment movement and removal of decomposition products [40]. However, the thermal stability of GO/Si_3N_4–EP

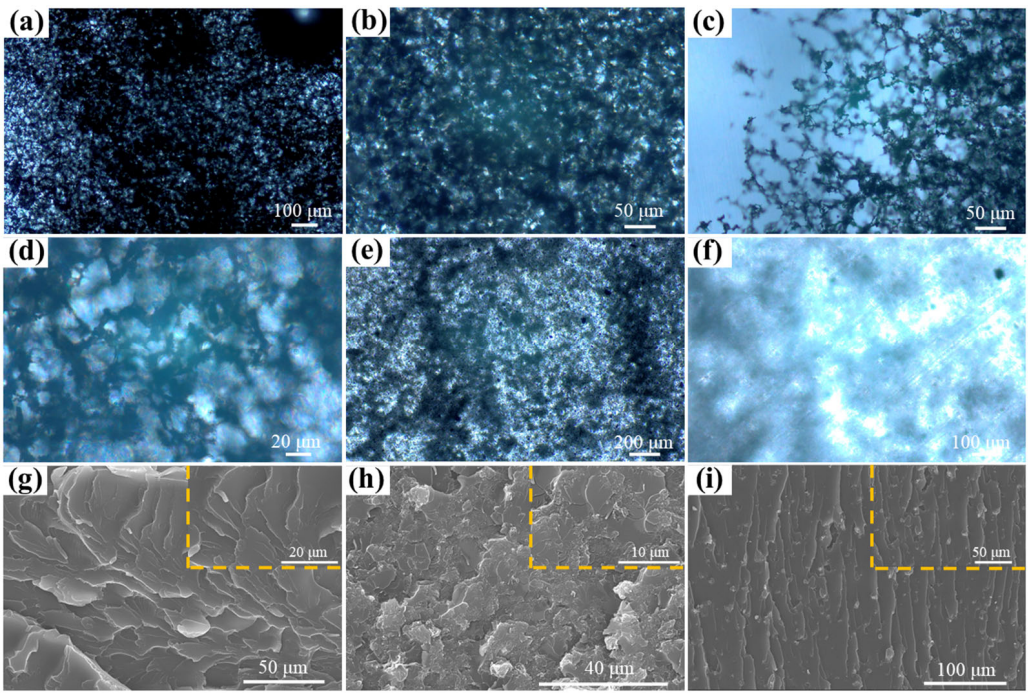

Fig. 4 Optical microscopy images of (a–d) $GSiA_1$–EP and (e, f) GO/Si_3N_4–EP; SEM cross-sectional morphologies of (g) EP, (h) $GSiA_1$–EP, and (i) GO/Si_3N_4–EP.

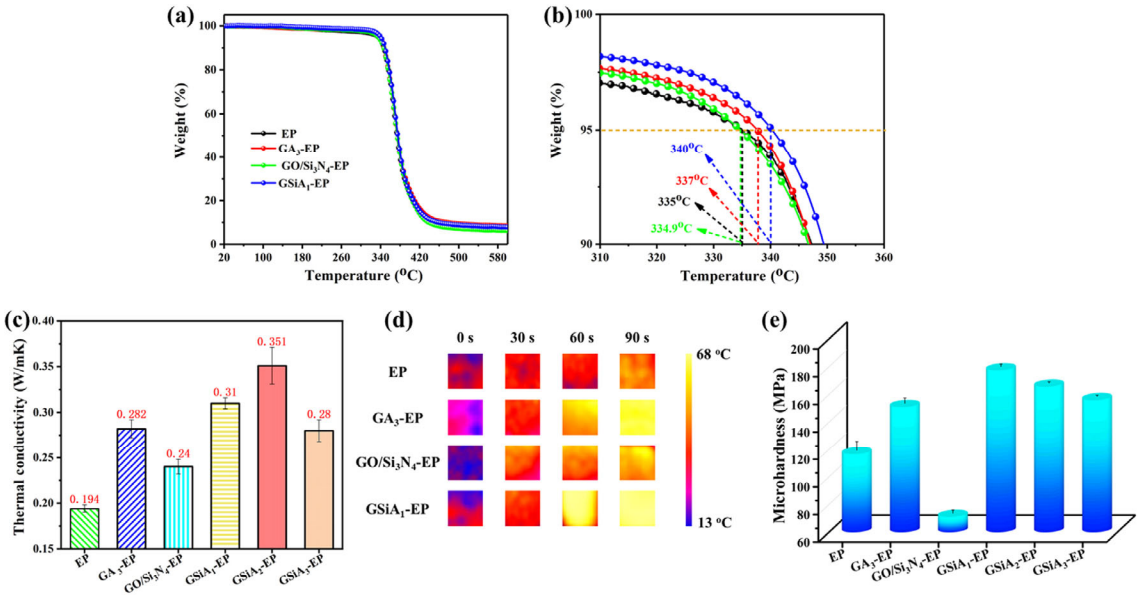

Fig. 5 Thermogravimetric analysis of (a) pure EP, GA_3—EP, GO/Si_3N_4—EP, and $GSiA_1$—EP; and (b) partial enlarged view of them; (c) thermal conductivity of different EP composites; (d) infrared thermal images of pure EP, GA_3—EP, GO/Si_3N_4—EP, and $GSiA_1$—EP; and (e) microhardness of pure EP, GA_3—EP, GO/Si_3N_4—EP, and GSiA—EP.

presented little effective enhancement compared to neat EP due to the serious agglomeration of GO sheets and Si_3N_4 whiskers.

Figure 5(c) depicted the thermal conductivity of EP, GA_3–EP, GO/Si_3N_4–EP, and GSiA–EP composites. Thereinto, due to the formation of effective 3D thermal network constructed by RGO sheets, the thermal conductivity of GA_3–EP was 0.282 W/mK, showing an increase by 45.4% compared to that of the neat EP. Furthermore, the thermal conductivity of $GSiA_1$–EP and $GSiA_2$–EP reached 0.31 and 0.351 W/mK, which presented a 60% and 81% increase compared to that of the neat EP, respectively. It could be described to that the Si_3N_4@PDA–PEI whiskers inside GSiA acted as the heat-conducting highways and bridges between the RGO sheets, which accelerated the heat diffusion and endowed the GSiA–EP composites with optimal thermal conductivity. But the excessive contents of Si_3N_4@PDA–PEI whiskers would result in poor thermal conduction performance due to the severe agglomeration and poor interfacial adhesion. In addition, compared with $GSiA_1$–EP, the thermal conductivity of GO/Si_3N_4–EP was decreased by 22.6%, indicating that the simple blending was difficult to form an effective heat conduction network inside EP.

Because it is generally believed that the large amount of fillers should be required to exceed the percolation threshold to form a thermal network by simple blending in the previous research work [41]. In order to observe the thermal conduction performance of different EP composites intuitively, all samples were placed onto a heating plate and the surface temperature was recorded by a thermal imaging camera. As displayed in Fig. 5(d), the surface temperature of $GSiA_1$–EP dramatically increased and firstly reached 68 °C after 90 s, which was faster than that of GA_3–EP and GO/Si_3N_4–EP. In contrast, the surface temperature of neat EP increased slowly to 41 °C at the same heating time due to its poor thermal conductivity. As a result, the $GSiA_1$–EP had the optimal thermal stability and thermal conductivity performance.

3.3 Microhardness

The Vickers hardness of neat EP and EP composites were shown in Fig. 5(e). It could be seen that the hardness of GA_3–EP, $GSiA_1$–EP, $GSiA_2$–EP, and $GSiA_3$–EP was 151.0, 177.4, 165.7, and 156.0 MPa, respectively, which was 29.4%, 48%, 42%, and 35.3% higher than that of the pristine EP. It was contributed to that the load could be effectively transferred through the 3D RGO/Si_3N_4 hybrid aerogel framework when subjected to the normal loading. In particular,

the matrix-filler adhesion could improve the hardness of $GSiA_1$–EP due to the great surface area and tremendous contact points caused by roughening the contact surface between the hybrid aerogel and polymer matrix. Besides, the reactive functional groups on the RGO sheets and Si_3N_4@PDA–PEI whiskers could produce the chemical reactions and promote the strong chemical bonding with the epoxy resin chains, which could make the chains of epoxy resin have a better resistance to external force [42]. By a contrast, the hardness of GO/Si_3N_4–EP was even lower than that of neat EP. It could be ascribed to that the RGO sheets and Si_3N_4 whiskers had an aggregation effect and then weaken the interface bonding between the fillers and epoxy resin, which could act as many mechanical weakness during the elastic deformation [43].

3.4 Tribological properties

Figure 6 conducted sliding tests to explore the effect of RGO/Si_3N_4 hybrid aerogel on the tribological performance of EP composites. The tribological properties of GA–EP with different GA were firstly investigated and shown in Figs. 6(a) and 6(b). It could be found that the average friction coefficient of GA_2–EP, GA_3–EP, and GA_4–EP was 0.33, 0.2934, and 0.3201, which was decreased by 5.8%, 16.2%, and 8.6% compared to that of the neat EP, respectively. In particular, the GA_3–EP had the lowest average friction coefficient, which could be ascribed to the continuous lubrication supply by 3D RGO sheets. The wear rate and wear width of GA–EP and neat EP were characterized in Fig. 6(b). Compared with the neat EP, the wear rate of GA_2–EP, GA_3–EP, and GA_4–EP was 7.083×10^{-5}, 4.67×10^{-5}, and 7.5×10^{-5} mm^3/(N·m), which was reduced by 49%, 66.4%, and 46%, respectively, which indicated that GA_3–EP had the optimal tribological properties. As for GSiA–EP composites, owing to the superior self-lubricating properties of RGO sheets and the outstanding load-bearing capacity of Si_3N_4@PDA–PEI whiskers, it could be seen that the friction coefficient of $GSiA_1$–EP was as low as 0.2249, presenting a decrease by 35.8% as compared to neat EP.

In contrast, the friction coefficient of GO/Si_3N_4–EP was higher than that of $GSiA_1$–EP, indicating that 3D cross-linked structure of $GSiA_1$ played an important role in the synergistic lubricating effect between RGO sheets and Si_3N_4@PDA–PEI whiskers. Perceptibly, compared to the simple blending of GO/Si_3N_4 fillers with EP, the 3D structure of $GSiA_1$ could effectively avoid the agglomeration of GO sheets and Si_3N_4 whiskers inside EP and promote the interfacial bonding between fillers and matrix. As a result, the

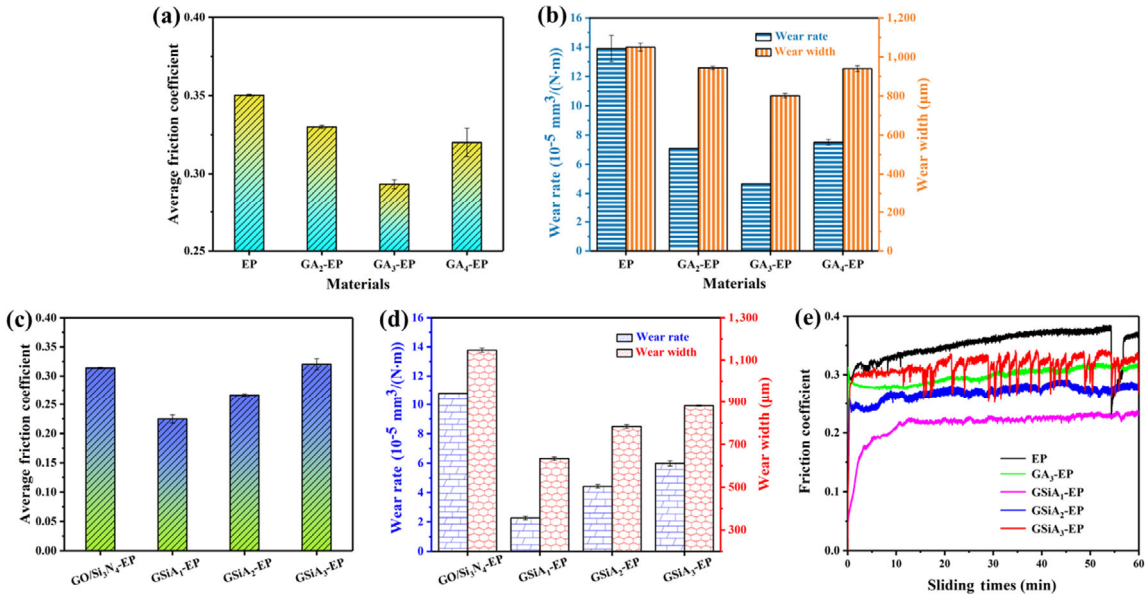

Fig. 6 Average friction coefficient of (a) pure EP and GA–EP, and (c) GO/Si_3N_4–EP and GSiA–EP composites; wear rate of (b) pure EP and GA–EP composites, and (b) GO/Si_3N_4–EP, GSiA–EP composites; (e) variation of the friction coefficients of pure EP, GA_3–EP, and GSiA–EP composites with time.

lubricating performance of GO sheets and carrying capacity of Si_3N_4 whiskers could be fully released to construct a high-quality transfer film. Furthermore, the excellent thermal properties of $GSiA_1$–EP could relieve the unexpected local softening of epoxy matrix and serious abrasion due to the friction heat. In the meanwhile, the wear rate of $GSiA_1$–EP reached the minimum value of 2.27×10^{-5} $mm^3/(N{\cdot}m)$, which was reduced by 83.7% compared to the pristine EP. It was worth noting that the wear rate of $GSiA_2$–EP and $GSiA_3$–EP tended to increase gradually with the further increase in the content of Si_3N_4@PDA–PEI whiskers. Even more remarkably, the wear rate of GO/Si_3N_4–EP was raised to 10.8×10^{-5} $mm^3/(N{\cdot}m)$, which was ~4.8 times higher than that of $GSiA_1$–EP. The above results implied that the $GSiA_3$–EP presented the optimal lubricating and abrasion resistance properties.

The coefficient of friction curves versus sliding time in the sliding process were exhibited in Fig. 6(e). The friction process could be categorized into two stages: running-in stage and steady state. The friction coefficient of all EP samples tended to increase sharply in the running-in stage. During steady state, the friction coefficient of neat EP was continuous to rise steadily. While the friction coefficient of GA–EP kept steady and was lower than the neat EP. Furthermore, the $GSiA_1$–EP had the most stable and the lowest friction coefficient. In contrast, with the increase of Si_3N_4@PDA–PEI whiskers content, the friction coefficient curve of $GSiA_2$–EP became unstable and the sever fluctuation was more obvious in $GSiA_3$–EP caused by the agglomeration of Si_3N_4@PDA–PEI whiskers.

3.5 Anti-wear mechanism

The morphologies of worn surfaces were used to investigate the anti-wear mechanism of various EP composites. Perceptibly, the wear area of pure EP was the highest among all EP composites (Fig. 7(a_1)). In particular, the worn surface was very uneven and rough (Fig. 7(a)), and a mass of delamination, cracks, and adhesive debris could be found on the worn surface (Fig. 8(a)), confirming the serious plowing damage and plastic deformation occurring in the sliding process. This phenomenon corresponded to the typical adhesive and fatigue wear, which could be attributed to the high brittleness and poor thermal properties of the pure epoxy resin [44]. As for GA–EP, it could be found that the wear area of GA_3–EP was narrower and the worn surface became relatively smooth (Figs. 7(b) and 7(b_1)). But some spalling pits, tiny wrinkles, and adhesive pits still appeared on GA_3–EP worn surface, corresponding to the slight adhesive wear and fatigue wear (Fig. 8(b)). As a contrast, the worn surfaces of GA_2–EP and GA_4–EP in

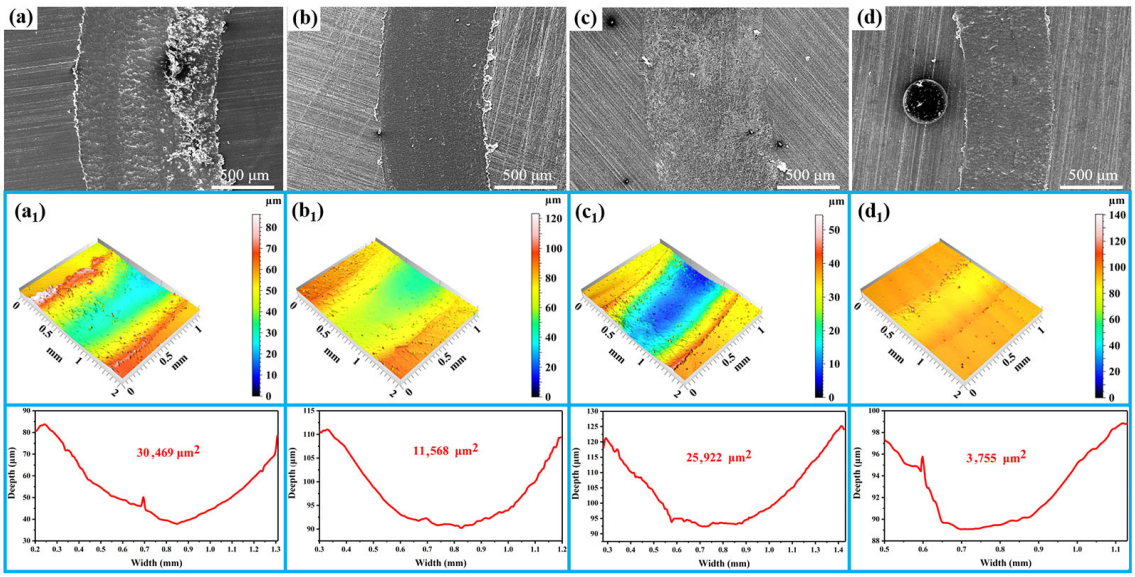

Fig. 7 SEM micrographs of the worn surfaces of (a) pure EP, (b) GA_3–EP, (c) GO/Si_3N_4–EP, and (d) $GSiA_1$–EP; (a_1–d_1) the corresponded 3D morphologies and the cross-section profile.

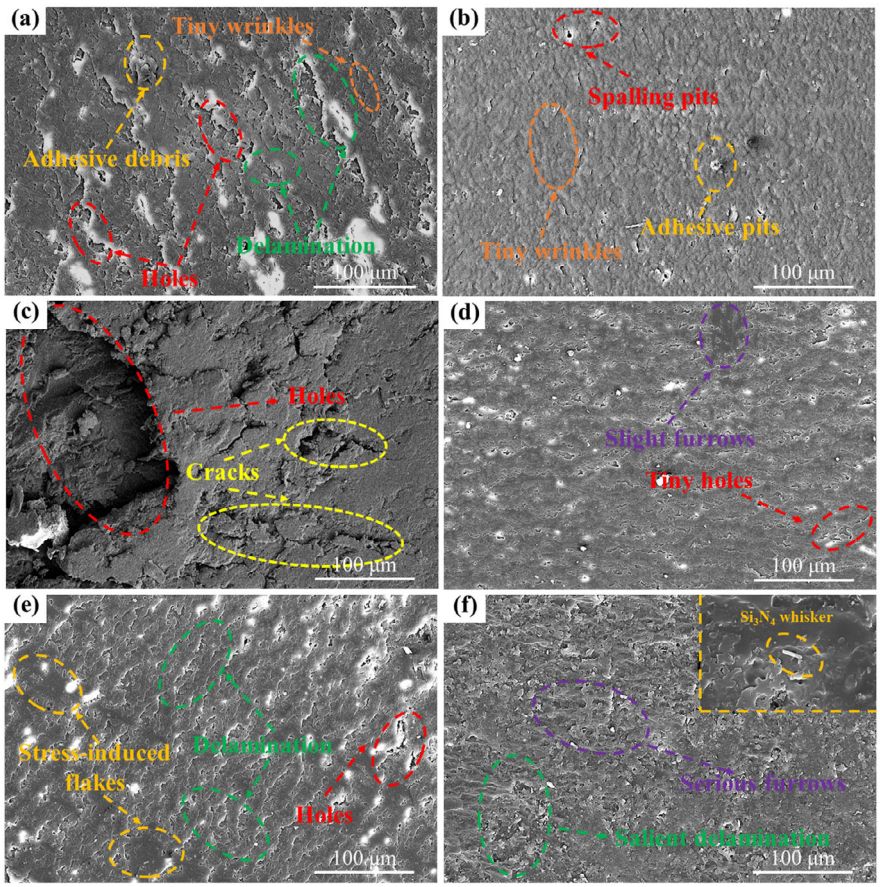

Fig. 8 SEM of the worn surface morphologies of (a) pure EP, (b) GA_3–EP, (c) GO/Si_3N_4–EP, (d) $GSiA_1$–EP, (e) $GSiA_2$–EP, and (f) $GSiA_3$–EP.

Fig. S5 in the ESM became more rough, proving the optimal anti-wear performance of GA_3–EP.

Specially, the $GSiA_1$–EP presented the lowest wear depth and the narrowest wear width (Figs. 7(d) and 7(d_1)), and no obvious adhesive trace except for some slight furrows and tiny holes could be found on its worn surface (Fig. 8(d)), corresponding to slight wear. By contrast, the wear area of GO/Si_3N_4–EP was obviously larger than that of $GSiA_1$–EP, the scratch surface was filled with serious holes and cracks corresponding to the serious adhesive wear and peeling wear (Fig. 8(c)). Compared to GO/Si_3N_4–EP, the RGO/Si_3N_4 hybrid aerogel with outstanding porous structure could elevate the dispersion of RGO sheets and Si_3N_4@PDA–PEI whiskers inside EP effectively, which could dissipate the friction heat timely through 3D heat conduction network. Moreover, the optimized interfacial interaction between hybrid aerogel and resin matrix could further improved the hardness of EP composites. Meanwhile, the improved dispersion and interfacial interaction contributed to a high-quality tribofilm by the continuous and steady replenishment of RGO sheets and Si_3N_4@PDA–PEI whiskers. However, the serious delamination and furrows could also be found on the $GSiA_2$–EP and $GSiA_3$–EP scratch surface (Figs. 8(e) and 8(f)), implying that the further increase in Si_3N_4@PDA–PEI whiskers content had a negative effect on anti-wear performance of EP matrix due to the unexpected agglomeration.

The wear morphologies and chemical composition of ball counterface after the friction process were characterized by SEM, Raman, and XPS analysis. As shown in Fig. 9(a), there was a thick and uneven transfer film formed on counterface corresponding to pure EP, indicating the rapid transfer and shedding of EP, which was consistent with severe abrasion of pure EP. As for GA–EP, the thin and flattened transfer film except for some cracks was found on counterpart surface, suggesting that the RGO sheets could participate in the friction transfer of EP and then

promote the bonding performance of transfer film (Fig. 9(b)). It was noteworthy that the counterpart surface was covered by a thin, uniform, and dense transfer film by $GSiA_1$–EP (Fig. 9(d)), which still remained flat and sturdy under the alternating stress. And the EDS results showed that the N and Si elements corresponding to Si_3N_4 whiskers were dispersed in the transfer film uniformly (Figs. 9(e) and 9(f)). However, the transfer film, uneven and loose, was formed by GO/Si_3N_4–EP, suggesting that the exposed Si_3N_4 whiskers were not easily attached to the steel ball surface (Fig. 9(c)), while the RGO sheets could contribute to the friction transfer of Si_3N_4@PDA–PEI whiskers through RGO/Si_3N_4 wrapping structure (Figs. 2(f)–2(h)). In summary, the combination of RGO sheets and Si_3N_4@PDA–PEI whiskers could improve the carrying capacity and bonding strength of transfer film effectively. The Raman spectroscopy (Fig. 9(e)) demonstrated that the I_D/I_G ratio of RGO in $GSiA_1$–EP was 1.14, while the transferred RGO sheets on countersurface was 0.84. It implied that the defect of RGO sheets could be slightly reduced and the structure of RGO sheets became more ordered due to the friction heat, which could display a significant tribological performance. That obtained results were consistent with the previous study [45]. Moreover, the XPS spectra were detected to further investigate the chemical composition of transfer film for $GSiA_1$–EP. High-resolution C 1s spectrum (Fig. 9(f)) indicated the presence of C=C/C–C (284.8 eV), C–OH (285.1 eV), C–O–C (286.5 eV) and C=O (288.4 eV), which were attributed to the epoxy resin, PDA–PEI copolymer, and the residual groups on RGO sheets. Furthermore, the N 1s could be divided into four peaks appearing at 395.7 eV (–N–C–), 397.5 eV (N–Si), 399.8 eV (–N–H), and $–NH_2$ (401.5 eV), respectively. Meanwhile, the Si 2p spectrum showed two peaks centered at 101.8 eV (Si–N) and 102.4 eV (Si–O–Si), which were attributed to the Si_3N4@PDA–PEI whiskers (Figs. 9(g) and 9(h)). Moreover, compared to the initial Si_3N_4@PDA–PEI whiskers (Fig. 3(h)), the peak intensities of Si–O–Si in Si 2p spectra of transfer film improved significantly, suggesting that some exposed Si_3N_4@PDA–PEI whiskers were oxidized to SiO_2 during the process of friction in air ambient. Different from the previous research [46], the oxidation rate of Si_3N_4@PDA–PEI

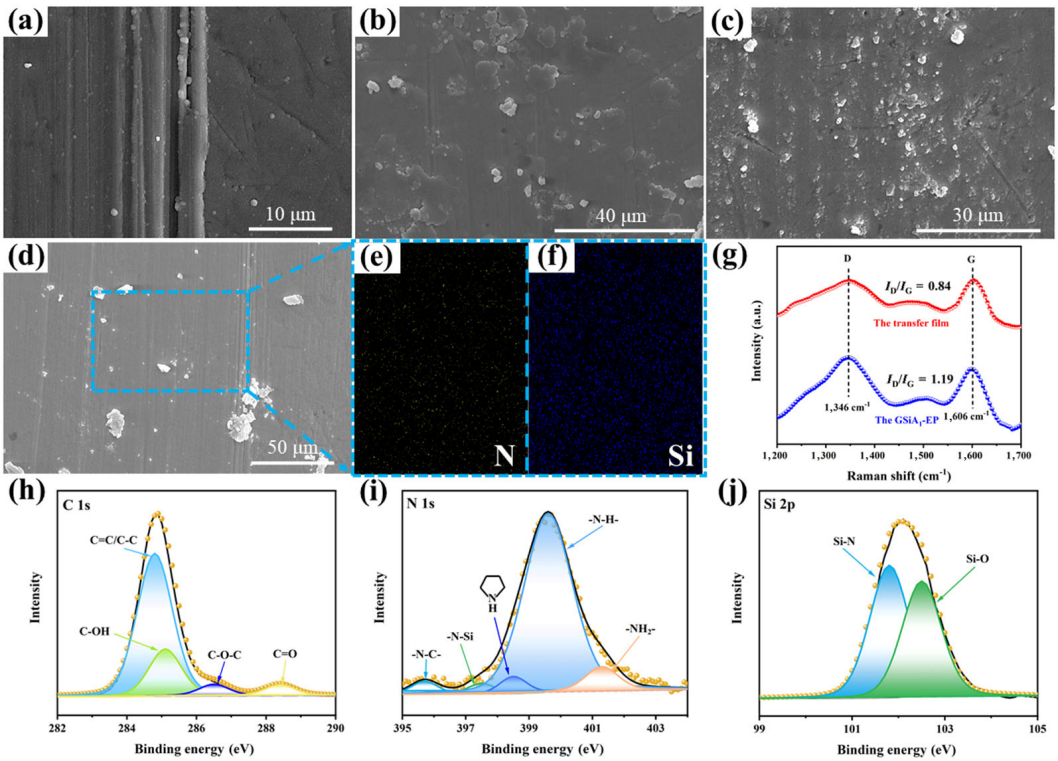

Fig. 9 SEM micrographs of the tribofilms of (a) pure EP, (b) GA_3–EP, (c) GO/Si_3N_4–EP, and (d) $GSiA_1$–EP; (e, f) EDS images of N and Si elements in the $GSiA_1$–EP; (g) Raman spectrogram of the pristine $GSiA_1$–EP and its tribofilm; (h–j) high-resolution XPS spectrum of C 1s, N 1s, and Si 2p for the tribofilm of $GSiA_1$–EP.

whiskers was faster, suggesting that the friction heat could offer energy for that chemical process to complete faster. This process could be presented in the reaction (2):

$$Si_3N_4 + 6H_2O \rightarrow 3SiO_2 + 4NH_3 \quad (2)$$

Hence, it implied that both of the releasing of RGO/Si_3N_4 wrapping hybrids and the production of SiO_2 could form the high-quality transfer film, greatly elevating the tribological performance of GSiA$_1$–EP.

Overall, the primary friction-reducing and anti-wear model of GSiA$_1$–EP could be seen in Fig. 10. As shown in Fig. 10(b), the 3D RGO/Si_3N_4 thermal network could dissipate timely the friction heat generated in the procedure of friction, which effectively avoided the large plastic deformation and local softening of epoxy matrix. Moreover, the RGO/Si_3N_4 wrapping hybrid could be transferred to the counterpart surface continuously and formed the high-quality transfer film, which avoided the direct contact between the hard steel ball and GSiA$_1$–EP composites (Fig. 10(c)). And the RGO sheets could further reduce the friction coefficient of GSiA$_1$–EP composites by interlayer gliding (Fig. 10(d)). As a result, the RGO/Si_3N_4 hybrid aerogel with 3D structure could endow the EP composites with optimal tribological properties.

4 Conclusions

In this work, we fabricated the reduced graphene oxide (RGO)/Si_3N_4 hybrid aerogel with fascinating three-dimensional (3D) porous structure via a facial hydrothermal and freeze-drying strategy. And the dispersibility of Si_3N_4@polydopamine–polyethyleneimine copolymer (PDA–PEI) whiskers was dramatically optimized through combination of wrapping of PDA–PEI and physical spacing of 3D skeleton. The 3D continuous conductive frameworks of RGO/Si_3N_4 hybrid aerogel endowed the epoxy resin (EP) composites with the better thermal conductivity. Furthermore, the thermal conductivity of GSiA$_3$–EP composites (the mass ratio of RGO flakes and Si_3N_4@PDA–PEI whiskers was 1:2) increased about 60% in comparison to that of the pure EP material. The specific wear rate and friction coefficient of GSiA$_1$–EP composites reached 2.27×10^{-5} (mm^3/(N·m)) and 0.2249, about 83.7% and 35.8% lower than that of pure EP material, respectively. Meanwhile, the GSiA–EP composites also possessed the excellent thermal stability and microhardness due to the physical blocking and interfacial interaction between RGO/Si_3N_4 hybrid aerogel and epoxy matrix. The results indicated that the prominent thermal properties, enhanced microhardness, and high-quality transfer films were responsible for the remarkable tribological performance of EP composites. Moreover, the successful obtained RGO/Si_3N_4 hybrid aerogel–EP composites would further widen the applications of epoxy resin composites in friction field.

Acknowledgements

The authors gratefully acknowledge the financial

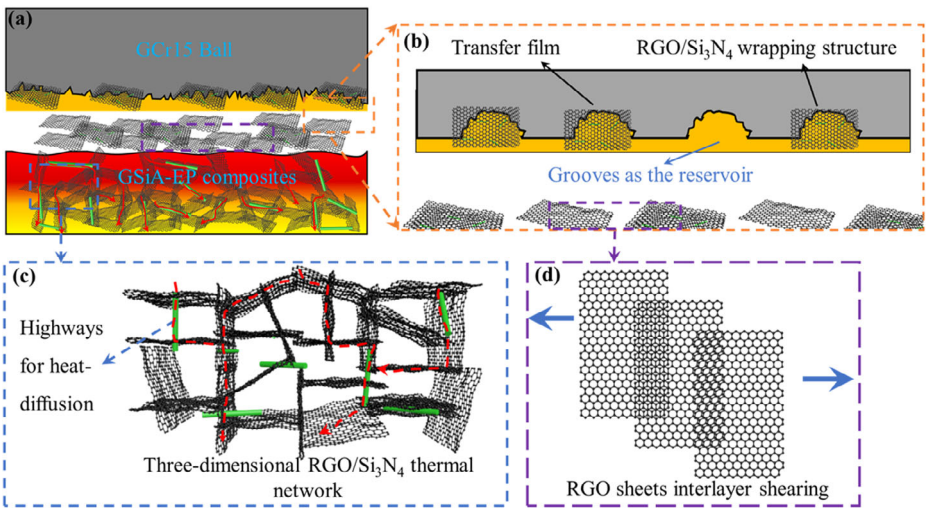

Fig. 10 Schematic diagram of the anti-friction and anti-wear mechanism of GSiA$_1$–EP composites.

support from the National Natural Science Foundation of China (Grant No. 52005487) and Natural Science Foundation of Gansu Province (Grant No. 20JR10RA057).

Declaration of competing interest

The authors have no competing interests to declare that are relevant to the content of this article.

Electronic Supplementary Material: Supplementary material is available in the online version of this article at https://doi.org/ 10.1007/s40544-022-0722-6.

References

[1] Gu H B, Ma C, Gu J W, Guo J, Yan X R, Huang J N, Zhang Q Y, Guo Z H. An overview of multifunctional epoxy nanocomposites. *J Mater Chem C* **4**: 5890–5906 (2016)

[2] Dong M, Zhang H, Tzounis L, Santagiuliana G, Bilotti E, Papageorgiou D. Multifunctional epoxy nanocomposites reinforced by two-dimensional materials: A review. *Carbon* **185**: 57–81 (2021)

[3] Jin F L, Li X, Park S J. Synthesis and application of epoxy resins: A review. *J Ind Eng Chem* **29**: 1–11 (2015)

[4] Lin Z, Jia X H , Yang J, Li Y, Song H J. Interfacial modification and tribological properties of carbon fiber grafted by TiO_2 nanorods reinforced novel depolymerized thermosetting composites. *Compos Part A-Appl Sci* **133**: 105860 (2020)

[5] Balguri P K, Samuel D G H, Thumu U. A review on mechanical properties of epoxy nanocomposites. *Mater Today* **44**: 346–355 (2021)

[6] Alanagh H R, Imani A, Zhang H, Owais M, Zhang X F, Zheng Y L, Mideksa M F, Tang Z Y, Zhang Z. Biomineralized coordinated metal polymers in epoxy for high mechanical and tribological properties. *Compos Part A-Appl Sci* **123**: 37–45 (2019)

[7] Liu C, Yin Q, Zhang W B, Bao Y, Li P P, Hao L F, Ma J Z. Tribological properties of graphene-modified with ionic liquids and carbon quantum dots/bismaleimide composites. *Carbon* **183**: 504–514 (2021)

[8] Zhang L L, Zhang Y, Zhu F Y, Zhao Z J, Yang Y, Sheng H C, Hou X H, Li H J. SiC nanowire−Si_3N_4 nanobelt interlocking interfacial enhancement of carbon fiber composites with boosting mechanical and frictional properties. *ACS Appl Mater Inter* **13**: 20746–20753 (2021)

[9] Lin Q L, Wang X, Cai M, Yan H, Zhao Z, Fan X Q, Zhu M H. Enhancement of Si_3N_4@MoS_2 core–shell structure on wear/corrosion resistance of epoxy resin/polyacrylate IPN composite coating. *Appl Surf Sci* **568**: 150938 (2021)

[10] Chen B B, Li X, Jia Y H, Xu L, Liang H Y, Li X F, Yang J, Li C S, Yan F Y. Fabrication of ternary hybrid of carbon nanotubes/graphene oxide/MoS_2 and its enhancement on the tribological properties of epoxy composite coatings. *Compos Part A-Appl Sci* **115**: 157–165 (2018)

[11] Han J H, Zhang H, Chu P, Imani A, Zhang Z. Friction and wear of high electrical conductive carbon nanotube buckypaper/epoxy composites. *Compos Sci Technol* **114**: 1–10 (2015)

[12] Eayal Awwad K Y, Yousif B F, Fallahnezhad K, Saleh K, Zeng X S. Influence of graphene nanoplatelets on mechanical properties and adhesive wear performance of epoxy-based composites. *Friction* **9**(4): 856–875 (2021)

[13] Liu C, Xi Li X, Lin Y, Xue X, Yuan Q M, Zhang W B, Bao Y, Ma J Z. Tribological properties of bismaleimide-based self-lubricating composite enhanced by MoS_2 quantum dots/graphene hybrid. *Compos Commun* **28**: 100922 (2021)

[14] Zhang Z N, Liu J, Wu T H, Xie Y B. Effect of carbon nanotubes on friction and wear of a piston ring and cylinder liner system under dry and lubricated conditions. *Friction* **5**(2): 147–154 (2017)

[15] Zhang N, Qu C H, Li S, Wang C K, Xu M K, Yang Z H, Zhang X R, Wang T M, Wang Q H. Significantly enhanced tribology and thermal management by dual-network graphene/epoxy composites. *Tribol Int* **164**: 107239 (2021)

[16] Li S, Dong C, Yuan C, Liu S, Bai X. Effects of CeO_2 nano-particles on anti-aging performance of HDPE polymer during friction. *Wear* **477**: 203832 (2021)

[17] Zhou Y J, Liu M, Wang Y L, Yuan J Y, Men X H. Significance of constructed MXene@Ag hybrids for enhancing the mechanical and tribological performance of epoxy composites. *Tribol Int* **165**: 107328 (2022)

[18] Eayal awwad K Y, Yousif B F, Fallahnezhad K, Saleh K, Zeng X S. Influence of graphene nanoplatelets on mechanical properties and adhesive wear performance of epoxy-based composites. *Friction* **9**(4): 856–875 (2021)

[19] Liu P F, Li X F, Min P, Chang X Y, Shu C C, Ding Y, Yu Z Z. 3D lamellar-structured graphene aerogels for thermal interface composites with high through plane thermal conductivity and fracture toughness. *Nanomicro Lett* **13**: 22 (2021)

[20] An F, Li X F, Peng Min P, Li H, Dai Z, Yu Z Z. Highly anisotropic graphene/boron nitride hybrid aerogels with long-range ordered architecture and moderate density for highly thermally conductive composites. *Carbon* **126**: 119–127 (2018)

[21] Gao Q, Qin J B, Guo B R, Fan X, Wang F P, Zhang Y, Xiao R L, Huang F, Shi X T, Zhang G C. High-performance electromagnetic interference shielding epoxy/Ag nanowire/thermal annealed graphene aerogel composite with bicontinuous three-dimensional conductive skeleton. *Compos Part A-Appl Sci* **151**: 106648 (2021)

[22] Karbasi M, Karimzadeh F, Raeissi K, Giannakis S, Pulgarin C. Improving visible light photocatalytic inactivation of E. coli by inducing highly efficient radical pathways through peroxymonosulfate activation using 3-D, surface-enhanced, reduced graphene oxide (rGO) aerogels. *Chem Eng J* **396**: 125189 (2020)

[23] Zhou H L Z, Wang H J, Du X S, Mo Y T, Yuan H, Liu H Y. Hybrid three-dimensional graphene fillers and graphite platelets to improve the thermal conductivity and wear performance of epoxy composites. *Compos Part A-Appl Sci* **123**: 270–277 (2019)

[24] Yang T T, Jiang Z Y, Han H M, Cai X Z, Liu Y Q, Zhang X R, Zhang X X, Ren Y J, Hu J. Welding dopamine modified graphene nanosheets onto graphene foam for high thermal conductive composites. *Compos B Eng* 205: 1108509 (2021)

[25] Ji C, Wang Y, Ye Z Q, Tan L Y, Mao D S, Zhao W G, Zeng X L, Yan C Z, Sun R, Kang D J, Xu J B, Wong C P. Ice-templated MXene/Ag–epoxy nanocomposites as high-performance thermal management materials. *ACS Appl Mater Inter* **12**: 24298–24307 (2020)

[26] Qin Y, Zhang Y, Qi N, Wang Q Z, Zhang X J, Li Y. The preparation of graphene aerogel with high mechanical stability and microwave absorption ability via combining surface support of metallic-CNTs and interfacial cross-linking by magnetic nanoparticles. *ACS Appl Mater Inter* **11**: 10409–10417 (2019)

[27] Cheng Y H, Liu Y X, An Y M, Hu N. High thermal-conductivity rGO/ZrB_2–SiC ceramics consolidated from ZrB_2-SiC particles decorated GO hybrid foam with enhanced thermal shock resistance. *J Eur Ceram Soc* **40**: 2760–2767 (2020)

[28] Zhou P, Yao D, Zuo K, Y Y, Yin J, Liang H, Zeng Y P. Highly dispersible silicon nitride whiskers in asymmetric porous separators for high-performance lithium-ion battery. *J Membr Sci* **621**: 119001 (2021)

[29] Ma X H, Qiao F F, Qian M, Ye Y Y, Cao X, Wei Y Y, Li N, Sha M L, Zi Z F, Dai J M. Facile fabrication of flexible electrodes with poly(vinylidene fluoride)/Si_3N_4 composite separator prepared by electrospinning for sodium-ion batteries. *Scripta Mater* **190**: 153–157 (2021)

[30] Wang T Y, Song Q, Zhang S Y, Li K, Xiao C X, Lin H J, Shen Q L, Li H J. Simultaneous enhancement of mechanical and electrical/thermalproperties of carbon fiber/polymer composites via SiC nanowires/graphene hybrid nanofillers. *Compos Part A-Appl Sci* **145**: 106404 (2021)

[31] Zong D D, Cao L T, Yin X, Si Y, Zhang S C, Yu J Y, Ding B. Flexible ceramic nanofibrous sponges with hierarchically entangled graphene networks enable noise absorption. *Nat Commun* **12**: 6599 (2021)

[32] Xiao C, Guo Y J, Tang Y L, Ding J W, Zhang X, Zheng K, Tian X Y. Epoxy composite with significantly improved thermal conductivity by constructing a vertically aligned three-dimensional network of silicon carbide nanowires/boron nitride nanosheets. *Compos B Eng* **187**: 107855 (2020)

[33] Logesh G, Sabu U, Srishilan C, Rashad M, Joseph A, Raju K C J, Balasubramanian M. Tunable microwave absorption performance of carbon fiber-reinforced reaction bonded silicon nitride composites. *Ceram Int* **47**: 22540–22549 (2021)

[34] Xuan C X, Li X Y, Wang Z, Wu H, Tang T, Wen J F, Li M, Xiao J R. Highly efficient polyaniline trapping and covalent grafting within a three-dimensional porous graphene oxide/helical carbon nanotube skeleton for high-performance flexible supercapacitors. *ACS Appl Energy Mater* **4**: 523–534 (2021)

[35] Wan Q, Tian J W, Liu M Y, Zeng G J, Huang Q, Wang K, Zhang Q S, Deng F J, Zhang X Y, Wei Y. Surface modification of carbon nanotubes via combination of mussel inspired chemistry and chain transfer free radical polymerization. *Appl Surf Sci* **346**: 335–341 (2015)

[36] Jiang Y, Chen Y, Liu Y J, Sui G X. Lightweight spongy bone-like graphene@SiC aerogel composites for high-performance microwave absorption. *Chem Eng J* **337**: 522–531 (2018)

[37] Kusunose T, Yagi T, H S, Firoz, Sekino T. Fabrication of epoxy/silicon nitride nanowire composites and evaluation of their thermal conductivity. *J Mater Chem A* **1**: 3440 (2013)

[38] Li D D, Huang J W, Huang L H, Tan S Z, Ting Liu T. High-performance three-dimensional aerogel based on hydrothermal pomelo peel and reduced graphene oxide as an efficient adsorbent for water/oil separation. *Langmuir* **37**: 1521–1530 (2021)

[39] Liu Q Y, Zhao Y L, Gao S S, Yang X, Rong Fan R, Zhi M Y, Fu M. Recent advances in the flame retardancy role of graphene and its derivatives in epoxy resin materials. *Compos Part A-Appl Sci* **149**: 106539 (2021)

[40] Yuan J Y, Zhang Z Z, Yang M M, Zhao X, Wu L F, Li P L, Jiang W, Men X H, Liu W M. Combined effects of interface modification and micro-filler reinforcements on the thermal and tribological performances of fabric composites. *Friction* **9**(5): 1110–1126 (2021)

[41] Gun-Ho K, Dongwook L, Apoorv S, Shao L, Min S K, David G, Jinsang K, Kevin P P. High thermal conductivity in amorphous polymer blends by engineered interchain interactions. *Nat Mater* **14**: 295–300 (2015)

[42] Davim J P. *Wear of Advanced Materials*. Hoboken (USA): John Wiley & Sons, Inc., 2013.

[43] Thooyavan Y, Kumaraswamidhas L A, Edwin Raj R, Binoj J S. Influence of SiC micro and nano particles on tribological, water absorption and mechanical properties of basalt bidirectional mat/vinylester composites. *Compos Sci Technol* **219**: 109210 (2022)

[44] Davim J P. *Tribology for Engineers*. Cambridge (UK): Woodhead Publishing, 2011.

[45] Zhao J, Li Q Z, Li S X, Li S C, Chen G Y, Liu X H, He Y Y, Luo J B. Influence of a carbon-based tribofilm induced by the friction temperature on the tribological properties of impregnated graphite sliding against a cemented carbide. *Friction* **9**(4): 686–696 (2021)

[46] Ru X, Hao J B, Zhang L C, Qian J S, Yuan X Y, LI B. Study on the surface structure of nano-and micro-silicon nitride in different atmospheres by FT-IR and XPS. *J Anhui Univ* **37**: 81–87 (2013)

Yongjun ZHOU. He received his bachelor degree from Taiyuan University of Technology, China, in 2020. He is currently a postgraduate student at School of Materials & Energy, Lanzhou University, China. His research interests focus on hybrid aerogel and carbon based epoxy self-lubricating composites.

Junya YUAN. He is currently working as an associate professor at Lanzhou Institute of Chemical Physics, Chinese Academy Science. He received his Ph.D. degree from Lanzhou Institute of Chemical Physics in 2019. His current research interests include the self-lubricating polymer composites and fabric liners, etc. He has published more than 40 papers in important journals and gained a number of patents.

Xuehu MEN. He is currently a professor at Lanzhou University. He received his B.S. degree from Lanzhou University in 2001 and the Ph.D. degree from Lanzhou Institute of Chemical Physics in 2009. His current research interests include the development of polymer composite materials and carbon based materials for lubrication and designing materials with special surface wettability. He is the author of more than 60 journal papers and several patent applications.